RUSSIAN JOURNAL *of* EARTH SCIENCES Online ISSN: 1681-1208

SPECIAL ISSUE: "KAMCHATKA EARTHQUAKE M 8.8 ON JULY 29, 2025"

COSEISMIC MULTIPLE CUSP SIGNATURES IN VIPIR IONOGRAMS FROM SKIKP-EXCITED INFRASOUND FOLLOWING THE 2025 M_W 8.8 KAMCHATKA EARTHQUAKE

J. Mabie[1], A. Skorkina[2], A. Molockova[2,3], T. Bullett[1], and S. Hollahan

[1]Fourth State Communications, Cheyenne, WY, USA
[2]Institute of Earthquake Prediction Theory and Mathematical Geophysics, Russian Academy of Sciences, Moscow, Russian Federation
[3]Moscow State University, Faculty of Physics, Moscow, Russian Federation
* **Correspondence to:** Justin Mabie, justin.j.mabie@gmail.com

Abstract: Following the M_W 8.8 Kamchatka earthquake on 29 July 2025, we observed coseismic Multiple Cusp Signatures (MCS) in successive 1-min ionograms recorded by the VIPIR ionosonde near Koror, Palau (PL407). We attribute these signatures to plasma displacements driven by three seismogenic infrasonic waves generated by teleseismic SKiKP phases. Doppler measurements reveal downward plasma displacements associated with each infrasonic wave. We further propose that the Palau barrier reef lagoon may serve as an efficient infrasonic wave generator, enabling MCS formation despite strong seismic attenuation over the ~4350 km epicentral distance.

Keywords: High altitude acoustic wave, coseismic ionospheric disturbance, SKiKP, ScS, Multiple Cusp Signature, VIPIR ionosonde, 2025 Kamchatka megathrust earthquake

Citation: Mabie J., Skorkina A., Molockova A., Bullett T., and Hollahan S. (2026), Coseismic Multiple Cusp Signatures in VIPIR Ionograms from SKiKP-Excited Infrasound following the 2025 M_W 8.8 Kamchatka Earthquake, *Russian Journal of Earth Sciences*, 26, ES2008, EDN: PLSNYR, https://doi.org/10.2205/2026es001128

RESEARCH ARTICLE

Received: February 2, 2026
Accepted: May 25, 2026
Published: July 1, 2026

1. Introduction

Earthquakes and tsunamis generate infrasonic waves (IWs) that can propagate upward into the ionosphere [*Davies and Baker*, 1965]. These IWs are overpressure anomalies in the neutral atmosphere; when they pass through the ionosphere, they displace plasma along their path. The displaced plasma can produce Multiple Cusp Signatures (MCS) in ionograms [*Maruyama et al.*, 2016]. MCS appear as localized increases in virtual height (range) and arise from the formation of a temporary plasma layer. The underlying mechanism involves a decrease in the index of refraction within this layer, which reduces the radio wave propagation speed and introduces range delay, manifesting as increased virtual height in the ionogram.

Historical ionograms from multiple stations have shown that Multiple Cusp Signatures (MCS) form after earthquakes of magnitude 8.0 or greater [*Maruyama et al.*, 2012], and after M_W 7.0 or greater when atmospheric conditions are favorable [*Rolland et al.*, 2011]. It has also been shown that MCS can occur following weaker events depending on earthquake type, atmospheric conditions, and epicentral distance [*Astafyeva*, 2019]. These MCS were initially attributed to infrasonic waves (IWs) generated by seismogenic Rayleigh waves with periods of tens of seconds [*Artru et al.*, 2004]. Subsequent studies have also associated coseismic ionospheric disturbances (CSID) with primary (P) and secondary (S) waves [*Chum et al.*, 2012]. The IWs propagate upward at the speed of sound and displace plasma downward as they pass through the bottom side ionosphere several minutes later [*Mabie and Bullett*, 2019].

Infrasonic waves (IWs) from non-seismic sources have also been shown to generate Multiple Cusp Signatures (MCS) in ionograms. Some physical properties such as propagation timing and plasma displacement, can be characterized using data from the Vertical Incidence Pulsed Ionospheric Radar (VIPIR) [*Mabie and Bullett*, 2019]. The VIPIR ionosonde enables measurement of plasma displacement velocities, derivation of accurate electron density profiles (EDPs), and in some cases, geolocation of MCS features, although the PL407 VIPIR doesn't currently make use of all of these capabilities. Atmospheric models provide sound speed profiles to estimate the propagation time and location of the IWs [*Mabie et al.*, 2016].

We apply a similar methodology to investigate coseismic Multiple Cusp Signatures (MCS) using the VIPIR ionosonde PL407 near Koror, Palau. In this study, we identify teleseismic SKiKP arrivals from the M_W 8.8 Kamchatka earthquake as the source of the three infrasonic waves (IWs) responsible for generating the observed MCS.

2. The M_W 8.8 Kamchatka Earthquake and Coseismic Multiple Cusp Signatures

The M_W 8.8 Kamchatka earthquake occurred at 23:24 UTC on 29 July 2025, with its epicenter at 52.3579°N, 160.5290°E at the depth of 43.7 km according to Kamchatka Branch of Geophysical Survey RAS (http://sdis.emsd.ru). The magnitude can be compared with the M_W 8.8 Maule (Chile, 2010) and M_W 9.0 Tohoku (Japan, 2011) earthquakes. Such earthquakes can produce strong ground motion in the epicentral zone, and also strong teleseismic arrivals.

Since there are no seismic stations close to the VIPIR ionosonde near Koror, Palau (PL407), we estimate theoretical travel times using the ak135 Earth model [*Kennett et al.*, 1995] for both Koror and Guam where the closest seismic station is located (Table 1). According to travel times computed using the ObsPy code (TauPyModel) and the ak135 Earth model, the S-wave arrived at the high-gain seismometer station GUMO (IU) on Guam, Mariana Islands (13.5893°N, 144.8684°E) at 23:38:44 UTC, followed by distinct ScS and SKiKP arrivals beginning around 23:42:39 and 23:45:15 UTC, respectively (Figure 1). ScS is S reflection from the core-mantle boundary, and SKiKP is S wave traversing the outer core as P, reflected from the inner core boundary and then continuing as P in the mantle (Figure 2). Both ScS and SKiKP are among 25 most reported teleseismic waves according to ISC [*Havskov and Lieser*, 2025], though SKiKP is a tricky phase which is often misidentified in bulletins [Table 5.1 in *Havskov and Lieser*, 2025].

Usually, both ScS and SKIKP onsets are quite short in time, but GUMO waveforms show that teleseismic waves formed by the long-period and slow source M_W 8.8 Kamchatka earthquake as long-period and long-lasting. Thus, according to accelerometer data, the source time function of the M_W 8.8 Kamchatka earthquake is 225 seconds long compared to 180 seconds for Maule and Tohoku (according to USGS). Moreover, seismic moment potential was mostly released in 60 (Tohoku) and 100 (Maule) seconds by two subfaults in each case, while the Kamchatka source consists of at least 4 subfaults with the strongest triplet among them [*Xu et al.*, 2025].

An outstanding fact is that for the distance of 4500 km, the SKiKP signal at the Guam high gain seismometer (GUMO-IU 10-BHZ) was saturated. It might be explained by interference of waves from subfaults or directivity. Another possible explanation for such a strong teleseismic arrival is that a significant part of energy was projected downward. Among other possible reasons, this could help explain the limited impact on the surface for such a large magnitude earthquake.

Several Rayleigh wave packets arrived at Guam beginning around 23:47 UTC, but these can be ruled out as sources of the infrasonic waves (IWs) responsible for the observed MCS. Their arrival at Palau would have occurred several minutes too late to account for the timing of the MCS in the 23:57 UTC and 23:58 UTC ionograms. Furthermore, the frequency content and packet structure of the Rayleigh waves do not match the characteristics of the three distinct IWs, which produced successive MCS features separated by less than one minute.

Table 1. Theoretical travel times for teleseismic phases at Guam and Koror

Phase	Path duration to GUMO (s)	Path duration to Koro (s)	Difference (s)	Apparent velocity (km/s)	Arrive at GUMO	Arrive at Koror
P	461.5	533.3	71.7	14.0	23:32:33.53	23:33:45.27
PP	555.5	648.0	92.4	10.9	23:34:07.54	23:35:39.95
PcP	582.5	613.8	31.3	32.1	23:34:34.49	23:35:05.77
S	832.4	963.0	130.6	7.7	23:38:44.39	23:40:55.01
SP	838.9	970.3	131.4	7.7	23:38:50.92	23:41:02.34
PS	840.4	971.8	131.4	7.7	23:38:52.41	23:41:03.76
SPP	845.4	977.6	132.2	7.6	23:38:57.37	23:41:09.59
PPS	846.9	979.0	132.2	7.6	23:38:58.86	23:41:11.02
PPPS	853.2	986.2	133.0	7.6	23:39:05.22	23:41:18.21
PkiKP	1011.3	1020.1	8.7	114.9	23:41:43.34	23:41:52.09
SS	1013.3	1175.5	162.2	6.2	23:41:45.35	23:44:27.54
SSP	1032.0	1180.8	148.8	6.8	23:42:04.00	23:44:32.80
PSS	1033.6	1182.4	148.7	6.8	23:42:05.62	23:44:34.37
SSS	1036.1	1256.2	220.2	4.6	23:42:08.10	23:45:48.25
SSSS	1049.1	1270.7	221.6	4.5	23:42:21.12	23:46:02.69
ScS	1066.9	1124.9	58.0	17.3	23:42:38.93	**23:43:36.92**
SkiKP	1223.2	1232.4	9.2	109.6	23:45:15.20	**23:45:24.38**
SkiKS	1436.3	1446.0	9.6	104.2	23:48:48.33	23:48:57.98

Figure 1 shows the seismogram recorded at Guam station GUMO during the arrival of the ScS and SKiKP phases. The seismogram counts represent the vertical velocity of solid-Earth displacement, with positive values indicating upward motion. Applying a simple acoustic model of a piston in an infinite baffle [*Bies et al.*, 2023], vertical surface motion generates pressure waves in the atmosphere whose intensity and period depend on the velocity and period of the ground displacement thrusts. The three prominent vertical displacement pulses, identified as SKiKP phases, are the suspected sources of the seismogenic infrasonic waves (IWs) that produced the observed MCS.

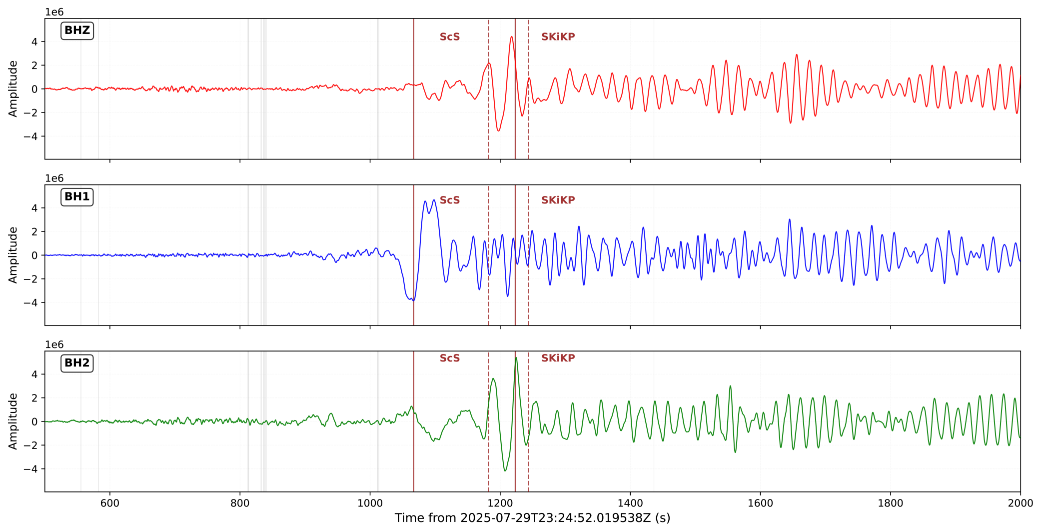

Figure 1. Three component seismogram from the high-gain station GUMO on Guam, showing theoretical travel times for body waves (grey lines). ScS and SKiKP are the most prominent onsets. The ScS time corresponds to the strongest amplitude on horizontal channel (BH1), while at SKiKP arrival time we see a few strong peaks on both vertical (BHZ) and horizontal (BH2) channels.

The solid Earth propagation paths for SKiKP and ScS body waves are shown in Figure 2. The relatively close arrival times for the SKiKP, ScS and surface Rayleigh wave phases, despite the different propagation path distances, account for the relatively high apparent velocity values of the SKiKP and ScS phases shown in Table 1.

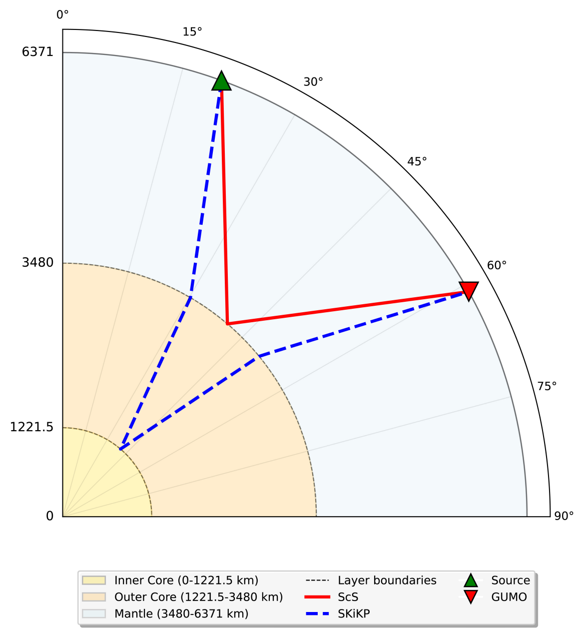

Figure 2. Travel paths for ScS (red solid line) and SKiKP (blue dash line).

A qualitative analysis of historical ionograms has led to the conclusion that Multiple Cusp Signatures (MCS) are typically caused by seismogenic infrasonic waves (IWs) for earthquakes of magnitude M_W 7.0 or greater when atmospheric conditions are favorable [*Rolland et al.*, 2011]. The 29 July 2025 Kamchatka Peninsula earthquake (M_W 8.8) clearly exceeds this threshold. However, the observation site over Koror, Palau, is approximately 4350 km from the epicenter. At such distances usually surface waves have the strongest amplitude, but for the M_W 8.8 Kamchatka earthquake, as we suppose because of source features, the SKiKP waves caused the strongest vertical motion. Also taking in account theoretical travel times, it is unlikely that surface waves have launched the observed IWs.

Previous investigations of coseismic ionospheric disturbances relied on measurement techniques less sensitive than the VIPIR and typically employed sounding intervals of 5–15 minutes, compared with the VIPIR's 1-minute cadence. As a result, the PL407 VIPIR is more likely to detect transient Multiple Cusp Signatures (MCS) than most conventional ionosondes.

3. SKiKP Arrival Times at Palau and Connection to MCS Observation Times

The SKiKP arrivals identified in Figure 1 required approximately 15 minutes to travel from the earthquake epicenter to Guam station GUMO, a great-circle distance of ~3840 km. According to the ak135 propagation model, the SKiKP phases arrived at Palau only about 10 seconds later than at Guam due to differences in ray path and station location (Table 1). The strongest SKiKP thrust was recorded at Guam at 23:45:15 UTC, and its estimated arrival at Palau is 23:45:33 UTC. By extension, the earlier strong thrust arrived at Palau at approximately 23:44:57 UTC (36 s earlier), and the third thrust at approximately 23:45:59 UTC (23 s later).

Infrasonic waves require 5–15 minutes to propagate from the surface to ionospheric altitudes where they can induce Multiple Cusp Signatures (MCS) in ionograms [*Mabie et al.*, 2016; *Maruyama et al.*, 2016]. Figure 3 shows the PL407 VIPIR ionogram recorded at 23:57 UTC, displaying three distinct MCS features. Figure 4 shows the ionogram from one minute later (23:58 UTC), in which two MCS remain visible, though less pronounced.

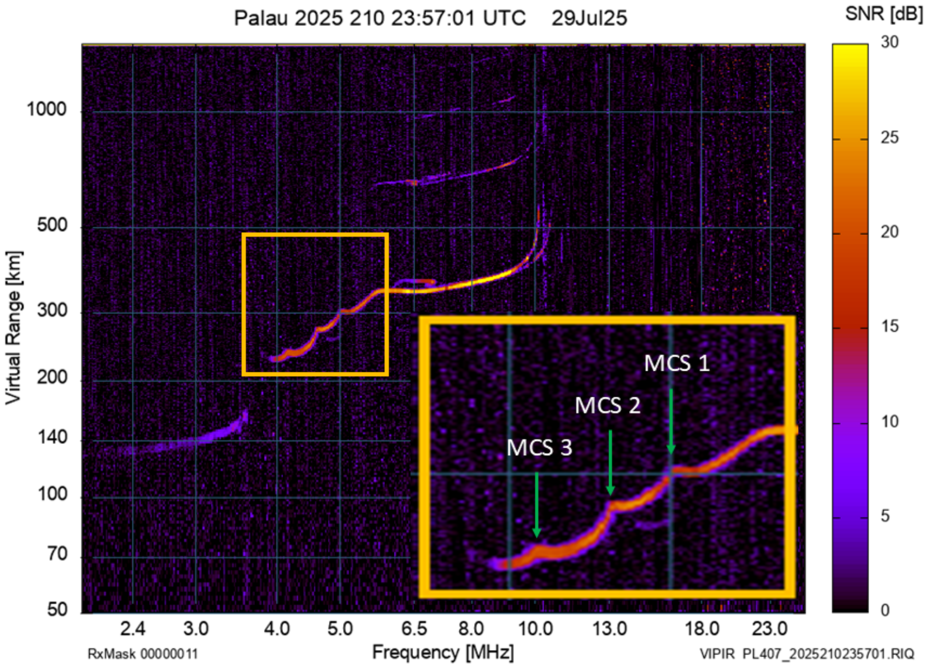

Figure 3. VIPIR ionogram recorded at PL407 (Koror, Palau) on 29 July 2025 at 23:57 UTC, showing three distinct Multiple Cusp Signatures (MCS) in the F-1 layer trace.

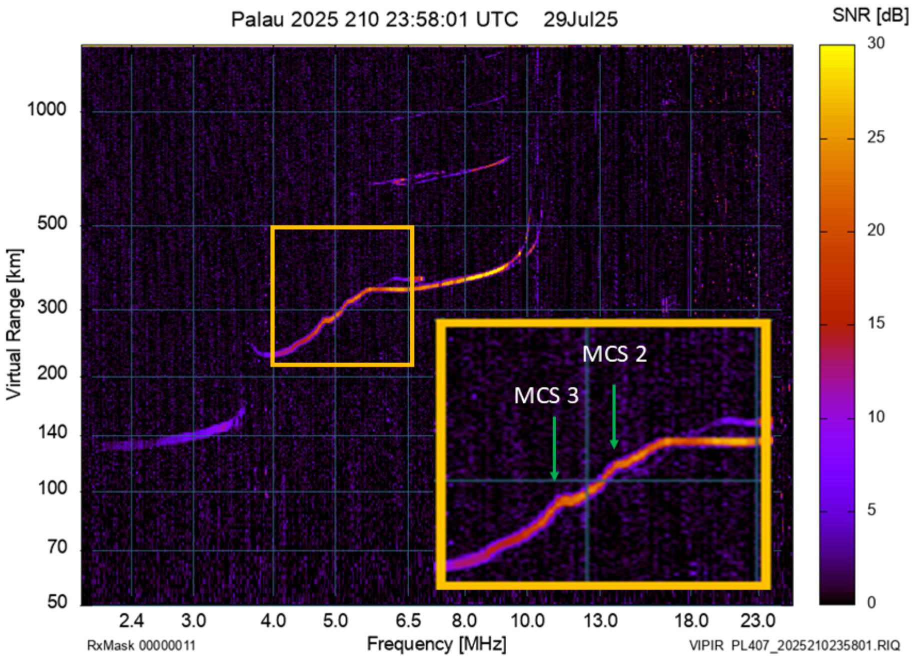

Figure 4. VIPIR ionogram recorded at PL407 (Koror, Palau) on 29 July 2025 at 23:58 UTC, showing two Multiple Cusp Signatures (MCS) induced by the same infrasonic waves responsible for features in the prior ionogram (Figure 3), though less pronounced.

For our analysis, we isolated the ionospheric echoes we are interested in. At each frequency and virtual range, signal power was calculated in decibels using a standard ionosonde formulation [*Mabie*, 2019b]. The strongest echo at each frequency was selected based on peak power, and the analysis was restricted to ranges between 100 km and 500 km to exclude non-F1-layer echoes.

Quality control was done by discarding unrealistic Doppler velocities (>40 m/s or having poor fit statistics) and removing outliers via Locally Weighted Scatterplot Smoothing (LOWESS), thereby eliminating false echoes and irrelevant returns (e.g., double-hop traces). Doppler velocities are derived by first computing the phase of the radar echoes and then calculating the change in phase over time [*Grubb et al.*, 2008; *Mabie et al.*, 2016].

Figure 5 presents Doppler velocity plots spanning 4–6 MHz, corresponding to the ionograms shown in Figures 3 (23:57 UTC) and 4 (23:58 UTC). We identified groundward plasma displacements that correspond to the MCS identified in Figure 3 and Figure 4, induced by three seismogenic infrasonic waves.

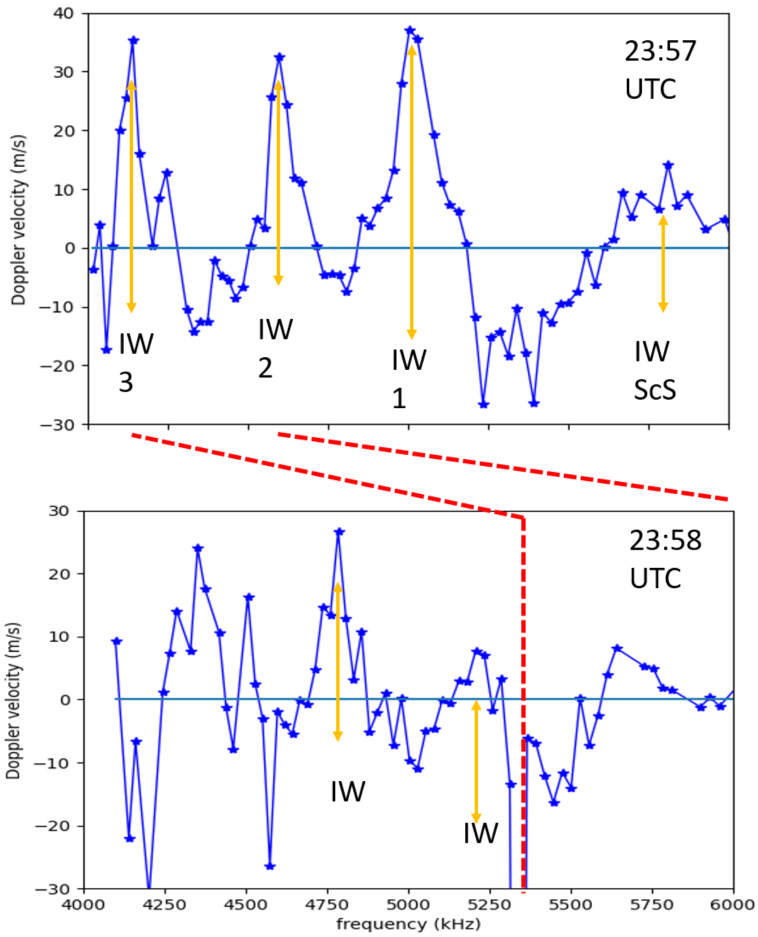

Figure 5. Doppler velocity spectra (4–6 MHz range) derived from VIPIR raw data for 23:57 UTC and 23:58 UTC, showing plasma displacements induced by all three SKiKP induced seismogenic infrasonic waves (IWs) and the ScS induced IW. Positive Doppler velocities indicate downward (groundward) plasma motion. The red dashed line shows the model projected frequency of IW3 and IW2 at 23:58, predicting faster IW propagation than what was observed.

There are three SKiKP induced coseismic IW signatures in the 23:57 UTC observation, but only two in the 23:58 UTC observation. The IWs displace both the plasma and the neutral atmosphere and the F-region becomes increasingly disturbed with time, resulting in only two MCS in the 23:58 UTC observation, and making it more difficult to identify plasma displacements caused by the third SKiKP induced IW during that observation. Increased variability in Doppler velocity values during the latter observation is a consequence of the more disturbed atmosphere.

4. Observation of an ScS induced IW

During the scope of our analysis of the SKiKP induced IWs, we noticed significant plasma displacements not associated with MCS occurred two minutes earlier. The magnitude of these plasma displacements approached 20 m/s compared to the typical atmospheric gravity wave induced plasma displacements on the order of 5 m/s beforehand [*Hines*, 1960].

Figure 6 shows the ionospheric Doppler velocities from 3 MHz to 7 MHz from 23:54 UTC and 23:55 UTC. An ScS induced IW is associated with the 10–20 m/s plasma displacements that appear at 23:55 UTC, two minutes before the SKiKP associated MCS are seen in the ionograms.

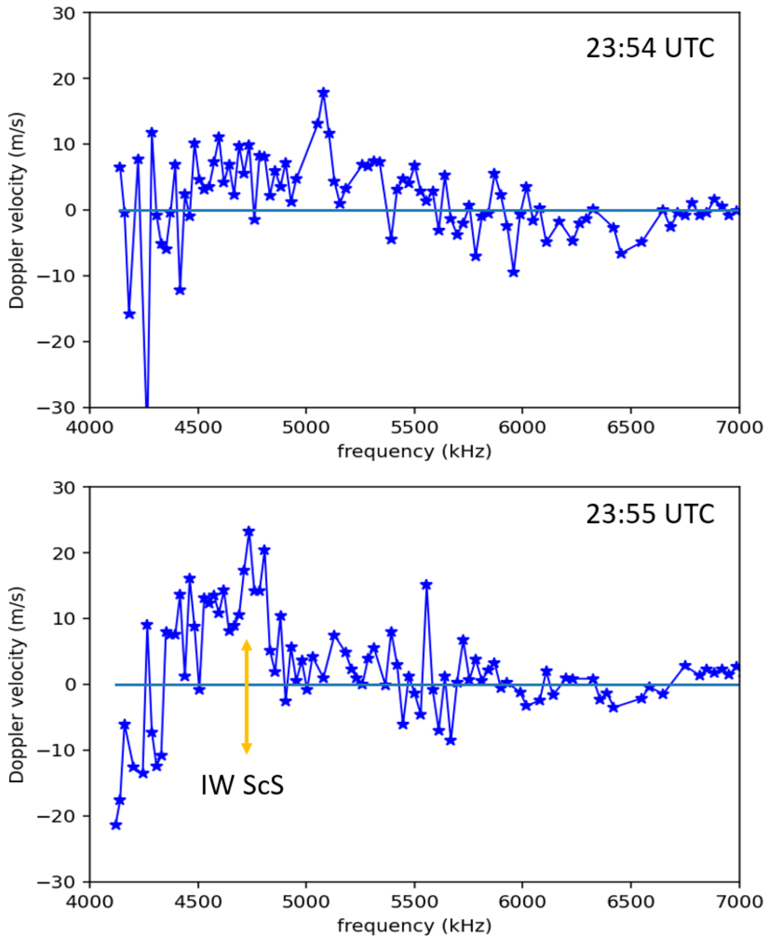

Figure 6. Doppler velocities showing a quiet ionosphere at 23:54 UTC, followed by 10–20 m/s plasma displacements at 23:55 UTC – two minutes before coseismic MCS are observed in the ionograms.

The identification of an ScS induced IW two minutes before the MCS are observed, is consistent with the timing of the arrivals shown in Table 1 where the ScS phase is computed to arrive one minute and forty-seven seconds earlier than the strongest SKiKP phase.

5. Tracking Infrasonic Waves in the Ionosphere

To link the infrasonic waves (IWs) responsible for the plasma displacements observed in Figure 5 to the SKiKP thrusts in Figure 1, we obtain plasma altitudes from the PyIRI EDP, and compute the time it takes for the IW to reach each altitude using the NRLMSIS temperature profile and Equation 1.

The EDP is given by the PyIRI International Reference Ionosphere model [*Forsythe et al.*, 2024], and the adiabatic speed of sound was computed from the NRLMSIS 2.0 temperature profile [*Emmert et al.*, 2021] using:

$$C = \sqrt{RT\frac{Cp}{Cv}}, \tag{1}$$

where Cp and Cv are the specific heats at constant pressure and volume, R is the ideal gas constant, and T is the absolute temperature. Propagation times from the surface to the altitudes of the observed plasma displacements were calculated numerically with 1 km altitude steps via:

$$t = \sum_{h=0}^{h'} \frac{dh}{C}$$

These observations are made around 9AM local time, about three hours after sunrise, when the thermosphere temperature and ionospheric plasma density is still increasing rapidly [*Verhulst and Stankov*, 2017]. This is a time of day where large errors are expected in both NRLMSIS and PyIRI profiles. Also, the PyIRI foF1 is at 4658 kHz, so the transition from the F-1 EDP to the F-2 EDP occurs in the middle of our observation region, adding complexity to the analysis.

Even if the conditions were more accommodating, it would be difficult to resolve the source of any error when simultaneously using a modeled sound speed profile and a modeled EDP. We recognize that the uncertainties in both models are not well quantified in the lower thermosphere, especially in the morning where thermospheric temperatures and electron densities are increasing rapidly. Uncertainty in PyIRI EDP values is typically around 10% [*Bilitza et al.*, 2022], and uncertainty in NRLMSIS temperatures values are on the order of 10–15% [*Picone et al.*, 2002].

A more ideal approach would be to use a high quality ionogram scaling tool like Dynasonde [*Zabotin et al.*, 2006], limiting model reliance to the thermospheric temperature profile. Such a tool was not available for this analysis.

Previously we reported an ionospheric IW mid-day using a high quality EDP scaled from a VIPIR observation [*Mabie*, 2019b] and computing sound speed using an NRLMSIS temperature profile. We showed that the IW propagation speed was well-behaved and consistent with the model sound speed profile, even at high altitudes when the rarefied atmosphere causes the adiabatic sound speed approximation to fail. Those results demonstrated that the model temperature profiles introduce bulk errors (e.g., propagation times over large distances) but that temperature dependent sound speed variations occur slowly compared to electron density profile variations that are characteristic of a highly structured ionosphere.

Applying the model results, we predict the IWs should propagate through the ionosphere much faster than was observed. Likely sources of error are 1) the NRLMSIS thermosphere temperatures are increasing too quickly 2) the slope of the PyIRI EDP is too steep, or 3) a combination of both.

There are two additional factors that should be considered. The VIPIR ionograms are represented in 'virtual range', which is the speed of light times propagation time. Because the radio waves are propagating through a plasma, their actual propagation speed is slower – so the real altitude is always less than the range shown in the ionogram, nominally 10%–30% lower under normal conditions [*Davies*, 1965]. At high altitudes (e.g., above 200 km depending on conditions), the thermosphere is sufficiently rarefied that the adiabatic sound speed propagation fails and IW propagation speed increases rapidly [*Mabie*, 2019b]. These combined factors suggest the NRLMSIS thermospheric temperature values are too high, and the actual IW propagation speed is slower than the computations predict. Consequently, the IWs probably took longer to reach the F-1 layer that the model predicts. This is supported by the ak135 SKiKP arrival times being one minute earlier than the back-calculated launch times.

6. Barrier Coral Reefs as Piston-like Acoustic Generators of Seismogenic Infrasound

For the M_W 8.8 Kamchatka Peninsula earthquake on 29 July 2025, teleseismic body waves (ScS and SKiKP) have unexpectedly stronger amplitudes than surface waves which are usually the strongest at such distances. Both this fact and travel time estimation made surface waves unlikely to generate the observed infrasonic waves. It should be noted, although SKiKP teleseismic body waves were identified as the most plausible source, such phases have not previously been linked to coseismic ionospheric disturbances, such as Multiple Cusp Signatures.

Our observations indicate that the acoustic generator producing the IWs was more efficient than sources typically associated with seismogenic IWs. We propose that the barrier coral reef acts as a highly efficient acoustic generator compared with a typical landmass. Figure 7 reproduces Darwin's model of coral reef formation [*Darwin*, 1842], illustrating the key concepts of this proposed mechanism.

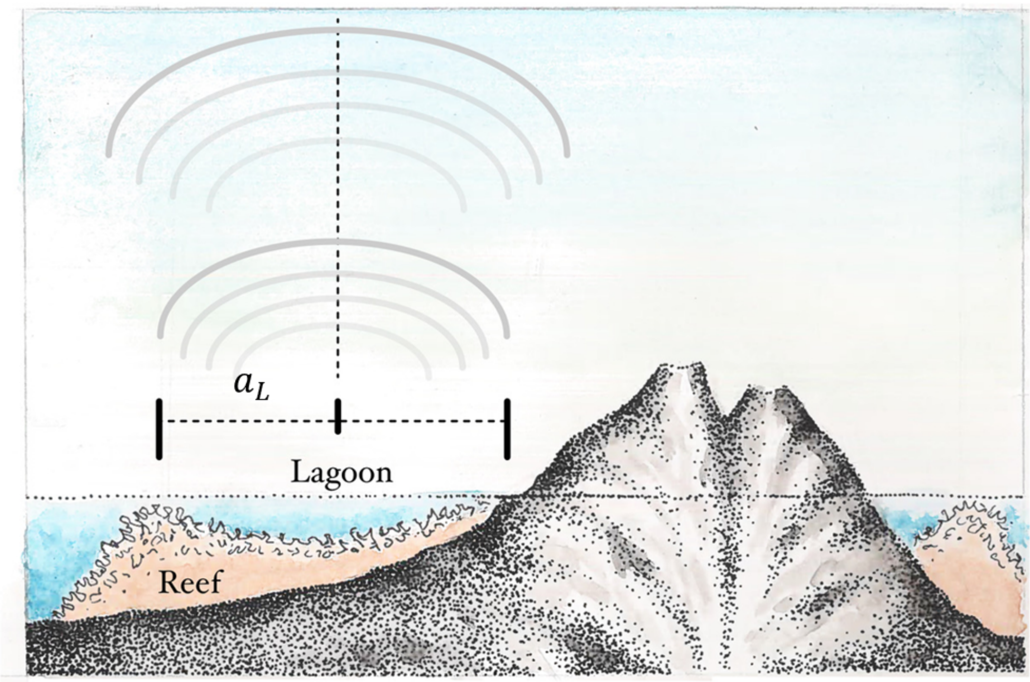

Figure 7. Model of a barrier coral reef based on Darwin's 1842 depiction. The lagoon with radius a_L has an ideal geometry to act as an efficient generator of coherent infrasonic waves.

Building on this conceptual model, we offer a theory to explain why the barrier coral reef lagoon outperforms a typical landmass as an infrasonic wave generator, treating the ocean surface above the reef as a piston in an infinite baffle. The proposed generator is the barrier reef and the flat ocean surface immediately above it, which oscillates vertically with the velocity and period of the seismic waves.

To evaluate the geometry of this model, we approximate the SKiKP-waves observed at Guam as monochromatic with a period of 36 s, corresponding to a wavelength of $\lambda = 343$ m and wave number $k = 0.0005$ rad/m. For a piston with a radius a, the generator is highly efficient when $k \cdot a > 1$, which holds for $a > 2$ km. The nominal diameter of the lagoon is 15 km (radius ~7.5 km), nearly four times the minimum required for efficient generation. In contrast, the large island of Babeldaob has a nominal diameter of about 10 km (radius ~5 km), more than twice the threshold, but its irregular, forested surface lacks the smooth, flat geometry needed for coherent radiation.

We approximate the ocean surface above the reef as flat, resulting in seismogenic infrasonic waves that are both monochromatic and coherent – an ideal condition rarely encountered in natural environments [*Bies et al.*, 2023].

The large island of Babeldaob is a hilly landmass covered by tropical forest. Because SKiKP waves propagate much faster in the solid Earth than the speed of sound in the atmosphere, vertically launched infrasonic waves (IWs) from different points on the island arrive at any given altitude with different phases. The resulting infrasound is monochromatic but incoherent, and the pressure and intensity of IWs from the island are lower than those from the lagoon.

The lagoon of the Palau barrier coral reef and the ocean surface directly above it satisfies the criteria for an ideal acoustic generator. Given the lagoon's large area and the relatively shallow, smooth ocean surface above it, we assume ideal free-field radiation impedance. The intensity of the infrasonic waves is proportional to the work they perform on the atmosphere, which is reflected in the magnitude of the plasma displacements observed in the ionosphere. In summary, the Palau barrier coral reef lagoon functions as an ideal generator of seismogenic infrasonic waves.

This ideal radiation impedance allows the lagoon to radiate infrasonic waves with maximum efficiency, converting a greater fraction of the seismic energy into coherent atmospheric pressure anomalies capable of reaching ionospheric altitudes. The Palau barrier coral reef lagoon thus provides a natural acoustic mechanism that explains the unexpected strength of the seismogenic infrasonic waves observed in this case, despite the attenuation of surface waves at large epicentral distance. This efficiency distinguishes barrier reefs from typical landmasses and may account for why coseismic MCS are occasionally detected over such environments when they would not be over continental or forested terrain.

7. Discussion

The observations presented here offer new insights into seismogenic infrasonic wave generation and ionospheric response. The presented results provide a foundation for future work, warranting a more in-depth discussion.

7.1. VIPIR Advantages and Sensitivity

The PL407 VIPIR ionosonde provided several critical advantages over traditional systems used in prior coseismic ionospheric studies. For example, operating with a 1-minute sounding interval, compared to the 5–15 minutes typical of historical ionosondes, the VIPIR captured the transient nature of the Multiple Cusp Signatures (MCS), which were present for only a couple of minutes in the F-layer.

High-gain amplifiers and ~1.5 km range resolution enabled detection of subtle plasma displacements that would likely have been missed by less sensitive instruments. This sensitivity allowed identification of Doppler velocities across 4–6 MHz, revealing three SKiKP induced and one ScS induced infrasonic waves.

These capabilities highlight the VIPIR's potential as a powerful tool for studying transient coseismic ionospheric disturbances, particularly in remote locations where high-resolution observations are otherwise limited.

7.2. Limitations and Approximations in the Analysis

In addition to large uncertainties in the model derived EDP and sound speed profiles, there are several important factors that we haven't fully considered. The far-field acoustic model treats the reef lagoon as a piston in an infinite baffle, but we lack detailed information on the generator's near-field properties and exact coupling to the atmosphere [*Bies et al.*, 2023]. Similarly, the adiabatic sound speed profile that uses the NRLMSIS 2.0 temperature profile, assumes constant Cp/Cv and neglects enhanced sound speeds in the rarefied upper atmosphere, introducing errors that increase with altitude in the thermosphere.

We also neglect changes in the slope of the EDP and plasma production and loss rates that are caused by vertical plasma motion. In particular, IW-induced downward plasma displacements increase recombination rates which alters the EDP [*Kakinami et al.*, 2012], and superposition of effects from vertical plasma displacements caused by multiple IWs further modify the EDP during the 23:57 UTC – 23:58 UTC window.

The observed downward plasma displacement is a result of the integrated pressure gradient force, with peak groundward velocity occurring after the IW peak has passed the layer. Thus, the actual IW altitude is above the plasma displacement location, adding uncertainty to back-calculated propagation times. These limitations highlight the need for more advanced models of IW-plasma interaction, and potentially including other factors such as geomagnetic field effects, and energy dissipation as horizontal TIDs are launched from vertical plasma displacements.

We also assumed that the IW propagation is vertical, neglecting any horizontal component, and we assumed a horizontally stratified ionosphere that neglects the spatial structure that determines where the transmitted radio waves reflect from, and we neglected any spatial variability in the IW induced plasma displacements. Simply, we performed a one-dimensional analysis on a complex three-dimensional system.

7.3. Hazard detection with real time observations of coseismic ionospheric disturbances

The transient nature of thermospheric IWs, also known as high-altitude acoustic waves (HAAWs) makes high time-resolution fixed-frequency Doppler sounders superior to traditional sweeping ionosondes for detecting and characterizing coseismic ionospheric disturbances. However, fixed-frequency systems are limited to discrete altitude sampling at the plasma frequency, restricting their ability to resolve vertical plasma displacements or estimate real altitudes without co-located ionosonde support.

To address these limitations, we have developed a "shuffle mode" for select VIPIR ionosondes, enabling simultaneous operation as a fixed-frequency Doppler sounder and a conventional ionosonde [*Mabie*, 2019a]. When coupled with EDP scaling, this hybrid capability provides altitude-dependent information and bulk displacement tracking while maintaining high sensitivity.

Implementing shuffle mode for real-time coseismic monitoring would require integrating automated alert systems to trigger mode changes upon detection of earthquake activity. Additional development is needed for seamless operating system integration and automatic re-initialization. Once operational, such systems could deliver near-real-time reports of coseismic ionospheric disturbances to end users.

In regions with sparse ocean buoy coverage, this capability could serve as an early tsunami detection method, potentially identifying signals minutes before traditional approaches. For example, VIPIR can detect IW induced plasma displacements in the E-layer (~100 km) up to several minutes earlier than GNSS TEC depletions near hmF2. Leveraging reduced D-region absorption from the overpressure anomaly, it is possible to detect the IW signature as low as ~50 km, significantly earlier than GNSS TEC depletions near hmF2 [*Mabie and Bullett*, 2019]. This framework offers a viable alternative for remote locations like Palau, where robust GNSS networks are absent.

7.4. Leveraging the interferometry capabilities of VIPIR

The VIPIR ionosonde transmits pulses with a radiation pattern extending up to ~45° off-vertical, conceptually similar to a flashlight beam. In a stratified ionosphere, echoes reflect from points where the wave normal is perpendicular to the layer tilt [*Zabotin et al.*, 2006], potentially up to ~250 km down-range at 250 km altitude. This wide coverage introduces spatial ambiguity in echo location absent interferometry.

Interferometry would allow precise mapping of the IWs. Downward displacement tilts the plasma layer toward the radar, creating a favorable reflecting surface that could be accurately located. The PL407 VIPIR is not currently configured for interferometry, precluding direct geolocation of the observed MCS features. However, this limitation is not critical for the present analysis.

The remote island chain setting and surrounding open ocean mean the IWs must originate nearby, as open ocean is a relatively poor acoustic generator except during tsunamis. We therefore conclude the MCS echoes are from overhead, and our timing and propagation results are unaffected by the absence of interferometric geolocation.

Future upgrades incorporating interferometry would significantly enhance VIPIR's utility for CSID studies, enabling spatial mapping of wave fronts and improving discrimination between local and distant sources.

8. Conclusion

This study presents coseismic Multiple Cusp Signatures (MCS) observed in successive VIPIR ionograms following the M_W 8.8 Kamchatka Peninsula earthquake on 29 July 2025. Three distinct MCS features, detected at PL407 near Koror, Palau, were directly correlated with individual SKiKP body-wave thrusts recorded at Guam, marking the first such linkage between MCS and teleseismic body waves rather than surface waves. Doppler velocities revealed downward plasma displacements from all three infrasonic waves (IWs), in addition to those caused by an ScS induced IW. Coseismic plasma displacements were observed across both the 23:57 UTC and 23:58 UTC observations, even as MCS visibility diminished in the later ionogram.

The M_W 8.8 Kamchatka earthquake with its unique long-lasting source time function – 225 seconds according to accelerometer data [*Xu et al.*, 2025] – generated an unusual set of teleseismic arrivals. Not only was SKiKP stronger amplitude than Rayleigh-wave phases, but also, we have seen at the Guam waveforms three SKiKP peaks which may have been generated by the three biggest subfaults of this mega-earthquake.

We propose that the Palau barrier coral reef lagoon served as an efficient, coherent infrasonic wave generator, modeled as a piston in an infinite baffle with ideal flat geometry and large radius ($k \cdot a \gg 1$), explaining the strong IWs despite weak seismic inputs and no reported shaking in Palau. This mechanism distinguishes barrier reefs from typical landmasses, where topographic phase variations and surface roughness produce incoherent radiation.

These results underscore the value of high-resolution VIPIR observations for transient coseismic ionospheric studies and highlight the potential of barrier reefs as natural amplifiers of seismogenic infrasound. Future work incorporating interferometry for CSID geolocation, real-time shuffle mode operation, and advanced IW-plasma interaction modeling will further enhance our understanding of these phenomena and their applications, including early tsunami detection in remote regions.

Acknowledgments. This work was supported by the Office of Naval Research and by ongoing institutional funding of IEPT RAS No. 075-00608-26-00. The authors thank the Coral Reef Research Foundation for field site support and the Government of the Republic of Palau for hosting our research activities.

References

Artru J., Farges T. and Lognonné P. Acoustic waves generated from seismic surface waves: propagation properties determined from Doppler sounding observations and normal-mode modelling // Geophysical Journal International. — 2004. — Vol. 158, no. 3. — P. 1067–1077. — https://doi.org/10.1111/j.1365-246x.2004.02377.x

Astafyeva E. Ionospheric detection of natural hazards // Reviews of Geophysics. — 2019. — Vol. 57, no. 4. — P. 1265–1288. — https://doi.org/10.1029/2019rg000668

Bies D. A., Hansen C. H., Howard C. Q., et al. Engineering Noise Control. — 6th. — CRC Press, 2023. — https://doi.org/10.1201/9780367814908

Bilitza D., Pezzopane M., Truhlik V., et al. The International Reference Ionosphere Model: A Review and Description of an Ionospheric Benchmark // Reviews of Geophysics. — 2022. — Vol. 60, no. 4. — https://doi.org/10.1029/2022RG000792

Chum J., Hruška F., Zednik J., et al. Ionospheric disturbances (infrasound waves) over the Czech Republic excited by the 2011 Tohoku earthquake // Journal of Geophysical Research: Space Physics. — 2012. — Vol. 117, A8. — https://doi.org/10.1029/2012JA017767

Darwin Ch. R. The structure and distribution of coral reefs. Being the first part of the geology of the voyage of the Beagle, under the command of Capt. Fitzroy, R.N. during the years 1832 to 1836. — London : Smith, Elder, Co., 1842.

Davies K. Ionospheric radio propagation. — U.S. Department of Commerce, National Bureau of Standards, 1965.

Davies K. and Baker D. M. Ionospheric effects observed around the time of the Alaskan earthquake of March 28, 1964 // Journal of Geophysical Research. — 1965. — Vol. 70, no. 9. — P. 2251–2253. — https://doi.org/10.1029/jz070i009p02251

Emmert J. T., Drob D. P., Picone J. M., et al. NRLMSIS 2.0: A Whole-Atmosphere Empirical Model of Temperature and Neutral Species Densities // Earth and Space Science. — 2021. — Vol. 8, no. 3. — https://doi.org/10.1029/2020ea001321

Forsythe V. V., Bilitza D., Burrell A. G., et al. PyIRI: Whole-Globe Approach to the International Reference Ionosphere Modeling Implemented in Python // Space Weather. — 2024. — Vol. 22, no. 4. — https://doi.org/10.1029/2023sw003739

Grubb R. N., Livingston R. and Bullett T. W. A new general purpose high performance HF Radar // Proceedings of XXIX General Assembly 7-16 august 2008. — Chicago, USA : URSI, 2008.

Havskov J. and Lieser K. Reported Teleseismic Phase Statistics at the ISC Over the Last Four Decades // Summary of the Bulletin of the International Seismological Centre. — 2025. — Vol. 58, no. II. — P. 31–44. — https://doi.org/10.31905/qea2ygg5

Hines C. O. Internal atmospheric gravity waves at ionospheric heights // Canadian Journal of Physics. — 1960. — Vol. 38, no. 11. — P. 1441–1481. — https://doi.org/10.1139/p60-150

Kakinami Yo., Kamogawa M., Tanioka Yu., et al. Tsunamigenic ionospheric hole // Geophysical Research Letters. — 2012. — Vol. 39, no. 13. — https://doi.org/10.1029/2011gl050159

Kennett B. L. N., Engdahl E. R. and Buland R. Constraints on seismic velocities in the Earth from traveltimes // Geophysical Journal International. — 1995. — Vol. 122, no. 1. — P. 108–124. — https://doi.org/10.1111/j.1365-246x.1995.tb03540.x

Mabie J. Infrasound induced plasma perturbations associated with geomagnetic pulsations // Russian Journal of Earth Sciences. — 2019a. — Vol. 19, no. 3. — ES3002. — https://doi.org/10.2205/2019es000661

Mabie J. Rocket Induced High Altitude Acoustic Waves : PhD thesis / Mabie J. — Boulder, 2019b.

Mabie J. and Bullett T. Infrasonic wave induced variations of ionospheric HF sounding echoes // Radio Science. — 2019. — Vol. 54, no. 10. — P. 876–887. — https://doi.org/10.1029/2019rs006826

Mabie J., Bullett T., Moore P., et al. Identification of rocket-induced acoustic waves in the ionosphere // Geophysical Research Letters. — 2016. — Vol. 43, no. 20. — https://doi.org/10.1002/2016gl070820

Maruyama T., Tsugawa T., Kato H., et al. Rayleigh wave signature in ionograms induced by strong earthquakes // Journal of Geophysical Research: Space Physics. — 2012. — Vol. 117, A8. — https://doi.org/10.1029/2012ja017952

Maruyama T., Yusupov K. and Akchurin A. Ionosonde tracking of infrasound wavefronts in the thermosphere launched by seismic waves after the 2010 M8.8 Chile earthquake // Journal of Geophysical Research: Space Physics. — 2016. — Vol. 121, no. 3. — P. 2683–2692. — https://doi.org/10.1002/2015ja022260

Picone J. M., Hedin A. E., Drob D. P., et al. NRLMSISE-00 empirical model of the atmosphere: Statistical comparisons and scientific issues // Journal of Geophysical Research: Space Physics. — 2002. — Vol. 107, A12. — https://doi.org/10.1029/2002ja009430

Rolland L. M., Lognonné P. and Munekane H. Detection and modeling of Rayleigh wave induced patterns in the ionosphere // Journal of Geophysical Research: Space Physics. — 2011. — Vol. 116, A5. — https://doi.org/10.1029/2010ja016060

Verhulst T. G. W. and Stankov S. M. Height-dependent sunrise and sunset: Effects and implications of the varying times of occurrence for local ionospheric processes and modelling // Advances in Space Research. — 2017. — Vol. 60, no. 8. — P. 1797–1806. — https://doi.org/10.1016/j.asr.2017.05.042

Xu D., Wang W. and Ren Z. Preliminary slip distribution of the July 29, 2025 M 8.8 Kamchatka, Russia earthquake // Earthquake Research Advances. — 2025. — P. 100427. — https://doi.org/10.1016/j.eqrea.2025.100427

Zabotin N. A., Wright J. W. and Zhbankov G. A. NeXtYZ: Three-dimensional electron density inversion for dynasonde ionograms // Radio Science. — 2006. — Vol. 41, no. 6. — https://doi.org/10.1029/2005rs003352